Nanoscale

PAPER

View Article Online
View Journal | View Issue

Cite this: *Nanoscale*, 2024, **16**, 16477

Extrinsic chirality tailors Stokes parameters in simple asymmetric metasurfaces†

Emilija Petronijevic, *[a] Tiziana Cesca,[b] Carlo Scian,[b] Giovanni Mattei,[b] Roberto Li Voti,[a] Concita Sibilia[a] and Alessandro Belardini[a]

Metasurfaces tailor electromagnetic confinement at the nanoscale and can be appropriately designed for polarization-dependent light–matter interactions. Adding the asymmetry degree to the desing allows for circular polarizations of opposite handedness to be differently absorbed or emitted, which is of interest in fields spanning from chiral sensing to flat optics. Here, we show that simple, low-cost asymmetric metasurfaces can control Stokes parameters in the transmitted far-field. With only 50 nm of asymmetric plasmonic shells on self-assembled polystyrene nanospheres, our metasurfaces allow for great spectral and incident angle tunability. We first investigated broadband extrinsic chirality in metasurfaces with asymmetric plasmonic semishells; we found high extinction circular dichroism (CD) in the near-infrared range. We then excited it with linear polarization and performed hyperspectral Stokes polarimetry on the transmitted field. We showed that the S_3 parameter follows the behavior of CD in extinction, and that the output field position on the Poincaré sphere can be widely controlled by using the incidence angle and wavelength. Furthermore, simulations agreed well with the experiments and showed how the near-field chiro-optical response influences the extrinsic chiral behavior in absorption and the polarization state of the transmitted field.

Received 29th November 2023,
Accepted 7th August 2024

DOI: 10.1039/d3nr06085c

rsc.li/nanoscale

[a]*Department SBAI, Sapienza University of Roma, Via A. Scarpa 14, I-00161 Rome, Italy. E-mail: emilija.petronijevic@uniroma1.it*
[b]*University of Padova, Department of Physics and Astronomy, NanoStructures Group, via Marzolo 8, I-35131 Padova, Italy*

† Electronic supplementary information (ESI) available. See DOI: https://doi.org/10.1039/d3nr06085c

Emilija Petronijevic

Emilija Petronijevic graduated from the University of Belgrade (Serbia), in physical electronics. She then did a PhD at La Sapienza University of Rome under the supervision of Prof. Sibilia. There, she studied the interaction of light with plasmonic, dielectric and hybrid nanostructures, focusing on the theory of chiro-optical response and phase-change materials. During her postdoctoral period, Emilija focused on related experimental work. Emilija's current interest lies in chiral properties at the nanoscale, directed towards novel chiro-optical functionalities and improved chiral sensing. She is currently a visiting researcher at the University of Bath, under the supervision of Prof. Valev.

1 Introduction

Plasmonic metasurfaces, made of nanoscale-structured plasmonic materials, offer remarkable properties regarding light–matter coupling, tailoring both near- and far-fields. While the near-field effects pave the way for highly efficient sensing platforms,[1–3] the directionality, polarization, intensity, and wavelength of the transmitted or emitted far-fields are potentially applicable in chip-scale components for flat optics and optical and quantum applications.[4–8] Breaking the symmetry of the electromagnetic interactions in metasurfaces enriches the fields of plasmonics and nanophotonics with chirality at the nanoscale.[9,10] Meta-atoms can be structured and organized to couple with chiral molecules for ultrasensitive chiral detection.[11–15] Moreover, as nanotechnology advances, nanophotonic and plasmonic communities propose nanostructured materials with remarkable chiro-optical control and polarization manipulation, which could potentially replace bulky optical components in chip-scale applications. Anisotropic nanoantennas were shown to convert polarization in telecoms[16] and the mid-infrared range,[8] while gap-plasmon-based metasurfaces have been applied in the determination of Stokes parameters[17] and intensity-tuneable metaholography *via* spin angular momentum selection.[18] Chiral meta-atoms have been further applied in chiral holographic displays,[19,20] for *in situ* tuneable circular dichroism by flexible substrates,[21] in Stokes

near-infrared[22] and mid-infrared polarimetry,[23] and for giant nonlinear chiro-optical effects.[24,25] Finally, sophisticated chiral metasurfaces, coupled with light nanosources, have been used for chiral single-photon emission[26] and spontaneous generation of vortex beams.[27]

Self-organization of matter into various chiral shapes is present in nature at all scales; this has inspired the fabrication of self-assembled single nanomaterials with structural 3D chirality and their complex assemblies.[28,29] On the other hand, coupling between single nanostructures on substrates opens up unprecedented chiral metasurface potentialities; for example, quasi-3D oligomers of Au and/or Ag led to broad chiral behaviour across the visible and near-infrared ranges,[30] while chiral single golden crescents, combined with hexagonal in-plane periodicity, opened up the field of chiral surface lattice resonances.[31] Nowadays, the vibrant field of chirality at the nanoscale would surely benefit from the simplification of nanoplasmonic geometries for multifunctional chiro-optical manipulation. Colloidal lithography has emerged as a fast, low-cost, and large-area manufacturing technique where nanosphere-based templates are used to obtain various plasmonic nanostructures based on nanoholes, shells, discs, and cones.[32–34] Nanosphere lithography (NSL) can be further combined with tilted metallic deposition to provide remarkable varieties of both asymmetric and chiral plasmonic metamaterials.[31,35–39] Self-assembled nanospheres form shadows during the plasmonic deposition, which can be used for simpler, 2D-chiral metasurfaces based on nanohole arrays.[40,41] Moreover, the metasurface does not need to be chiral itself in order to exhibit chiro-optical effects: instead, they can be induced in asymmetric (but not chiral) metasurfaces, by appropriately exciting the metasurface at oblique incidence. Such an effect is called "extrinsic" chirality,[42–44] and it allows for largely tuneable near- and far-field chiro-optical interactions.[45–47] We previously used nanosphere-based lithography (NSL) to obtain samples with asymmetric plasmonic shells that can be manipulated *via* extrinsic chirality. We showed that such samples, at oblique incidence, differently interact with left and right circular polarizations (LCP and RCP), thus exhibiting circular dichroism (CD) in absorption,[48] diffraction,[49] and extinction.[50] Self-assembled asymmetric plasmonic nanocrescents were also applied for SERS amplification[51] and for efficient second harmonic generation exhibiting CD.[52]

In this study, we show how thin asymmetric plasmonic shells efficiently tailor extrinsic chiro-optical interactions in metasurfaces, leading to hyperspectral control of the transmitted beam polarization state. The low-cost sample has simple geometry, which allows for the broad CD resonance in the near-infrared range. We start with experimental and numerical investigations of the extrinsic chirality. We then excite the sample with linear polarization and perform broadband analysis of the Stokes parameters in the transmitted field. The S_3 parameter, which indicates the circular polarization degree, follows the extinction CD, and agrees with the rules of extrinsic chirality.[53] Moreover, the polarization state is widely tuneable with respect to wavelength and incidence angle.

2 Results and discussion

2.1 Sample geometry and experimental setup

The investigated metasurface consists of polystyrene nanospheres (PSNs) asymmetrically covered by gold, lying on a soda-lime glass substrate. We aimed to investigate asymmetric plasmonic shells with resonances in the near infrared range. Therefore, we combined NSL and tilted metal deposition to obtain asymmetric geometry and 2D arrangement, as explained in our previous works.[48–50] However, in this work, we aimed to avoid the formation of nanohole arrays[54] on the substrate in order to obtain simpler geometry and overall higher transmission. We started from self-assembled PSNs of 522 nm diameter, and we decreased their diameter by reactive ion etching to around 370 nm, while preserving 2D periodicity. Next, we induced the asymmetry by a tilted evaporation of 50 nm of Au at 60° (*i.e.*, along the second nearest neighbour direction, as sketched in Fig. 1); this angle and diameter choice prevents the nanohole formation, which occurred in the case of evaporation at 45° in our previous works.[48–50] Fig. 1a and b show a scanning electron microscopy (SEM) image of the sample, and a simplified 3D model, respectively. Fig. 1c shows a top-view schematic of the rectangular unit cell used, with the definition of the average in-plane asymmetry vector $\vec{s}$: this is the average direction of Au deposition, projected onto the *xy* plane. The $\vec{s}$ vector is crucial in performing the extrinsic chirality characterization, as it must make a non-planar triad of vectors with the surface normal, and wavevector of the incoming light.[55] Extrinsic chirality was investigated in reflection and transmission from sophisticated metasurfaces fabricated by electron beam lithography.[56,57] Here,

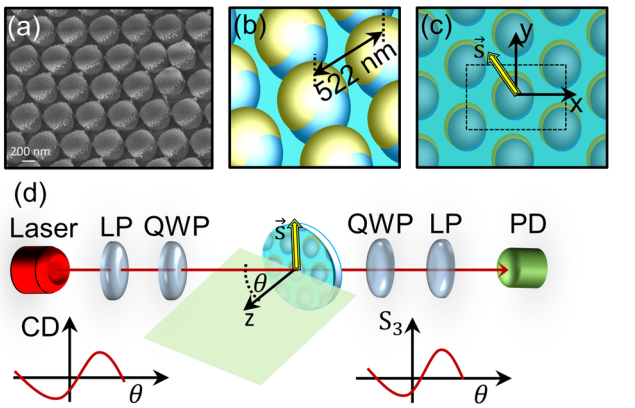

Fig. 1 (a) SEM image of the sample. (b) 3D schematic model for 60° deposition. (c) The *xy* cross-section of the numerical model showing the offset between the hexagonal unit cell symmetry, and the average golden shell direction in the *xy*-plane. (d) Experimental setup for the full analysis of the extinction chirality and the broadband angle-dependent Stokes parameter characterization.

instead, we used cost- and time-efficient fabrication to obtain an ordered sample over a large area (mm^2). NSL is based on commercially available PSNs, without relying on cleanroom facilities and multiple precise nanofabrication steps. Finally, we were able to obtain large-area metasurfaces, where plasmonic layer of only 50 nm introduces the asymmetry which allows for the control of near- and far-field chiro-optical effects, as further shown.

Fig. 1d presents the experimental setup for characterization of extrinsic chirality in extinction, and for full Stokes polarimetry of the transmitted field. We used a widely tuneable near-infrared laser (Chameleon Ultra II by Coherent Inc.) for excitation in the 720–1060 nm range. We used it in linear mode, with appropriately decreased output power.[50,54] A first block, made of a linear polarizer (LP) and a rotating quarter-wave plate (QWP), controls the polarization state of the input beam between left-handed circular polarization (LCP), right-handed circular polarization (RCP) or linear p-polarization (with respect to the green incidence plane). The sample was rotated so that the incidence plane stays perpendicular to the $\vec{s}$ vector. In extinction measurements, the total zeroth order transmission was recorded using a Si photodiode (PD) and normalized to the transmission through air without the sample. For the characterization of full Stokes parameters, another block with a QWP followed by an LP was put on the path of the transmitted field; for each wavelength and incidence angle, four combinations of QWP–LP orientations were used to resolve the S parameters. Definitions of the input polarization states and Stokes parameters are explained in detail in the ESI.†

2.2 Extrinsic chirality in extinction

We first excited the sample with LCP and RCP polarizations and measured the total extinction as $\mathrm{Ext}_{\mathrm{LCP,RCP}} = 1 - T_{\mathrm{LCP,RCP}}$, where $T_{\mathrm{LCP,RCP}}$ is the transmittance when the sample is excited with LCP or RCP, respectively. Fig. 2 shows the measured extinction CD, defined as:

$$\mathrm{CD_{ext}}[\%] = 100\frac{\mathrm{Ext_{LCP}} - \mathrm{Ext_{RCP}}}{\mathrm{Ext_{LCP}} + \mathrm{Ext_{RCP}}}, \quad (1)$$

which has a dependence on the angle of incidence θ and wavelength λ. A broad CD peak reaching around ±15% appears in the 900–1000 nm range for the absolute value of angles larger than 20°. With respect to NSL-obtained samples with nanoholes on the substrate,[50] this metasurface provides a simpler $\mathrm{CD_{ext}}$ map, with features governed by a single resonance in the 800–1000 nm range. As expected in extrinsic chirality experiments, CD inverts the sign with inversion of the incidence angle. However, we note that the broadband CD behaviour is not perfectly antisymmetric with respect to normal incidence. We attribute this to intrinsic chirality[58–60] (see below) and to the fact that we define the incidence plane with respect to the $\vec{s}$ vector, which does not necessarily lie parallel to the lines of hexagonal symmetry.

To understand the electromagnetic coupling in the near-field and the origin of extrinsic CD, we modeled the metasurface in a commercial 3D finite-difference time domain (FDTD) solver by using Lumerical.[61] The model takes into account only the asymmetric Au semishells on periodic PSN (tilted by 60°), without the residual metal deposition on the substrate; details of the model are given in the ESI.† The simulated extinction CD, reported in Fig. 2, closely follows the measured one in the near-infrared range: for the best fit, the $\vec{s}$ vector is rotated by 30° with respect to the y-direction of the FDTD domain, thus accounting for both intrinsic and extrinsic chirality. As this model correctly reproduces the extinction experiments in our wavelength range, we further use it to investigate the origin of the broad absorption. The metasurface exhibits a broad plasmonic resonance of the asymmetric shell at around 1000 nm, as shown in Fig. 3a; note that this absorption slightly differs for LCP and RCP excitation, due to intrinsic chirality. Oblique incidence by an angle θ with respect to the sample normal splits the resonances and decreases the RCP (LCP) absorption at $\theta = -30°$ ($\theta = +30°$). Such large differences can be appreciated by looking at the distribution of the absorption density in one unit cell, as shown in Fig. 3b. LCP light at 1000 nm and $\theta = -30°$ strongly couples with the plasmonic asymmetric semishell, leading to a similar peak in the extinction, and further producing large positive CD (Fig. 2).

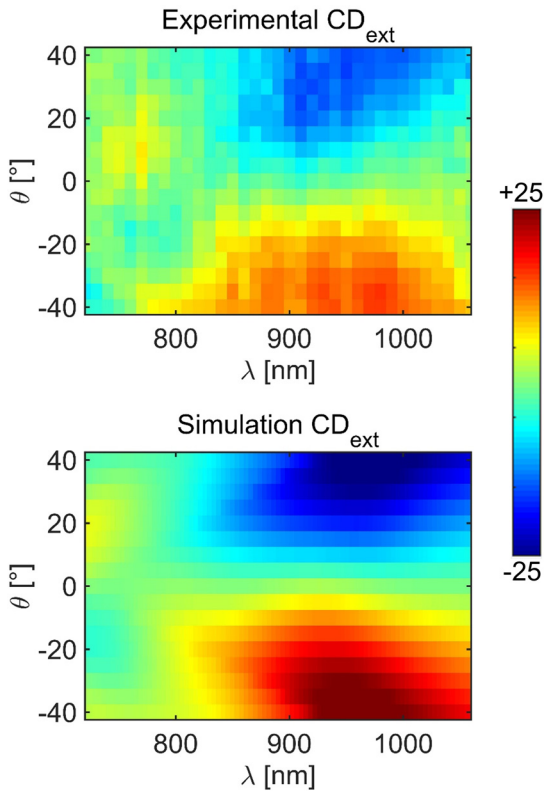

Fig. 2 Experimental and simulated extinction CD as a dependence on the incidence wavelength and angle.

2.3 Extrinsic chirality and Stokes parameters

Since the metasurface differently absorbs LCP and RCP under oblique incidence, we further investigated the polarization

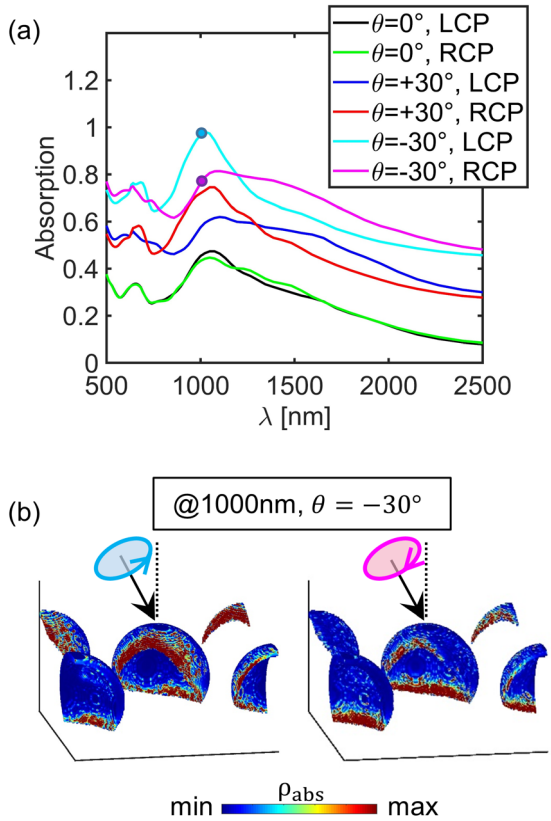

Fig. 3 (a) Calculated absorption shows extrinsic chiral behaviour resonating at around 1000 nm; for the sake of clarity, θ = +30° and θ = −30° lines are vertically shifted by 0.2 and 0.4, respectively. (b) Excitation at 1000 nm resonance leads to a large difference in the absorption density between LCP and RCP for θ = −30°.

control of the transmitted field. The excitation is p-polarized, lying perpendicular to the $\vec{s}$ vector. In the output, we resolve the Stokes parameters by appropriately orienting the second QWP–LP pair. Here, the Stokes parameters S_1 and S_2 show the prevalence of linear polarizations: horizontal with respect to vertical (S_1), and diagonal +45° with respect to −45° (S_2). More importantly, S_3 describes the dominance of RCP with respect to LCP, while all three parameters are normalized to the total intensity (S_0). Without the sample, p-polarized excitation corresponds to S_1 = 1 (horizontal).

We first measured the Stokes parameters at 800 nm as a function of the incidence angle (Fig. 4a). At this wavelength, there are no particular CD resonances; the red dots represent CD_{ext} measured in the same λ–θ configuration. S_1 becomes only slightly decreased and converted into S_2 and S_3. On the other hand, Fig. 4b plots the Stokes parameters and CD_{ext}, measured at the broad resonance of 1000 nm. Here, at oblique incidence, linear polarization is strongly converted into right elliptical polarization for negative θ, and into left elliptical polarization for positive θ. S_3 remarkably follows the behaviour of CD_{ext}, while at normal incidence, the polarization state remains unaffected. We next fixed the incidence angle and controled the wavelength. Fig. 4c shows the wavelength tuning

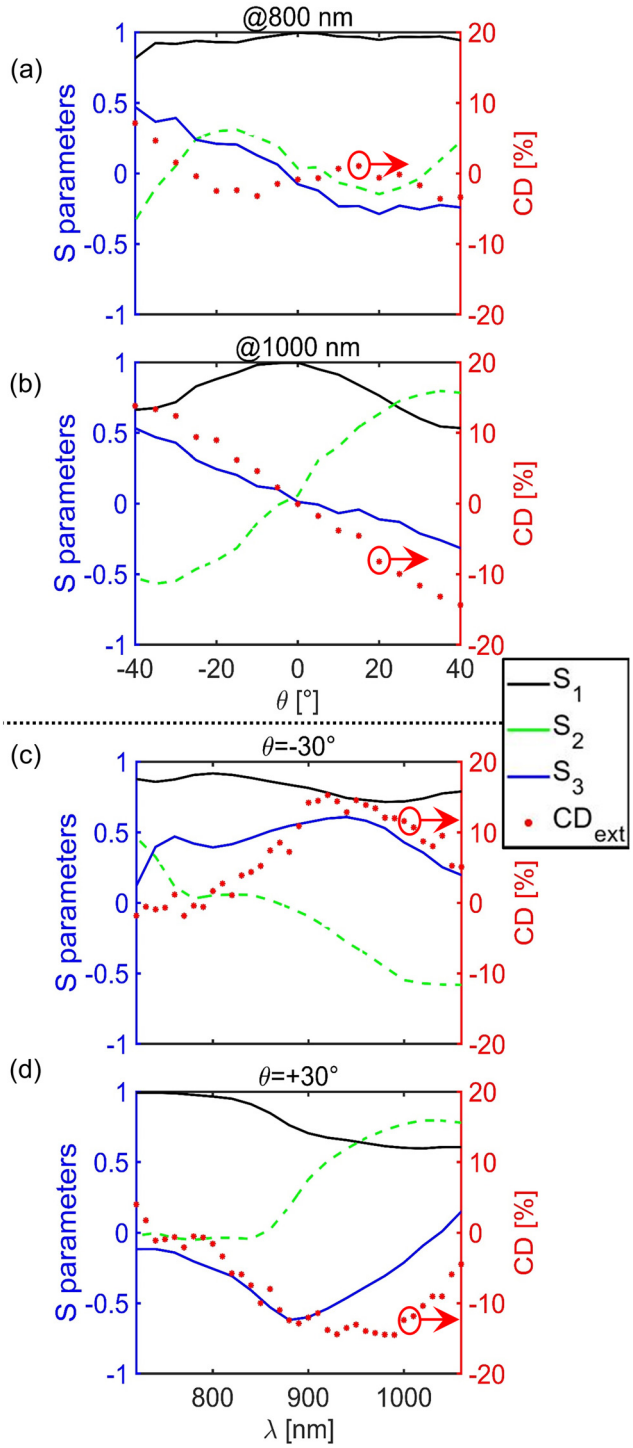

Fig. 4 (a) S parameters of the output light, when the metasurface is excited with p-polarized light, and its comparison to the extinction CD for incidence angle rotation at (a) 800 nm and (b) 1000 nm; (c and d) tuning the excitation wavelength for (c) θ = −30° and (d) θ = +30°.

of the polarization state at oblique incidence, θ = −30°. Over the whole wavelength range, S_3 agrees with CD_{ext}. Interestingly, below 750 nm, while CD_{ext} is negligible, S_3 decreases with decreasing wavelengths, while S_2 increases. Similarly, above

1000 nm, while both CD_{ext} and S_3 decrease with increasing wavelengths, S_2 increases in the absolute value; this could be a signature of optical rotation. Finally, Fig. 4d is close to the mirror image of Fig. 4c for S_3 and CD_{ext}. Therefore, with the inversion of the incidence angle, extrinsic chirality flips the handedness of the transmitted beam.

Furthermore, we fully characterized the Stokes parameters in the 720–1060 nm range for the incidence angles from θ = −40° to θ = +40°. Fig. 5 clearly shows the conversion of the incident linear polarization into the elliptical and broadband tuning of this effect across different incidence angles. As S_1 decreases in broad near-infrared regions for $|\theta| > 20°$, S_2 and S_3 increase in absolute values, and with opposite signs. Again, neither of the three maps is antisymmetric, due to the influence of the intrinsic chirality. Interestingly, S_3 follows the CD_{ext} map from Fig. 2. This can be explained by representing the linear polarization as an equal combination of LCP and RCP. At oblique incidence, *e.g.*, for negative angles, LCP becomes strongly absorbed; hence, CD_{ext} is positive, and so is the S_3 parameter, indicating that the transmitted light is predominantly right in ellipticity.

2.4 Versatile polarization evolution

We further represented the evolution of the polarization state at different wavelengths, as the sample is rotated. Fig. 6 shows the path of the polarization state on the Poincaré sphere when the incidence angle θ is changed. In the near-infrared range, for excitation configurations around the CD_{ext} resonance, different elliptical polarization states can be finely tuned. At 880 nm, the decrease of the parameter S_1 transfers to the

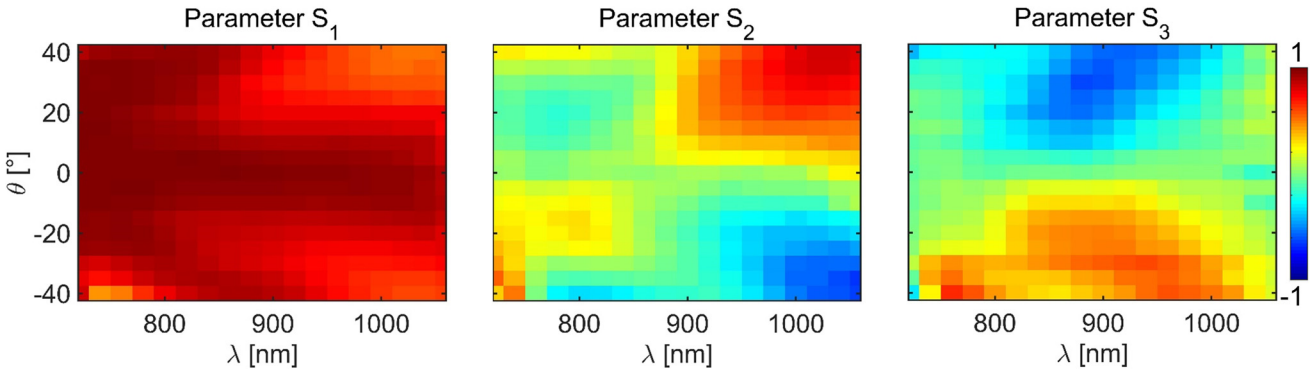

Fig. 5 Full characterization of the *S* parameters of the transmitted light, dependent on the excitation wavelength λ and incidence angle θ.

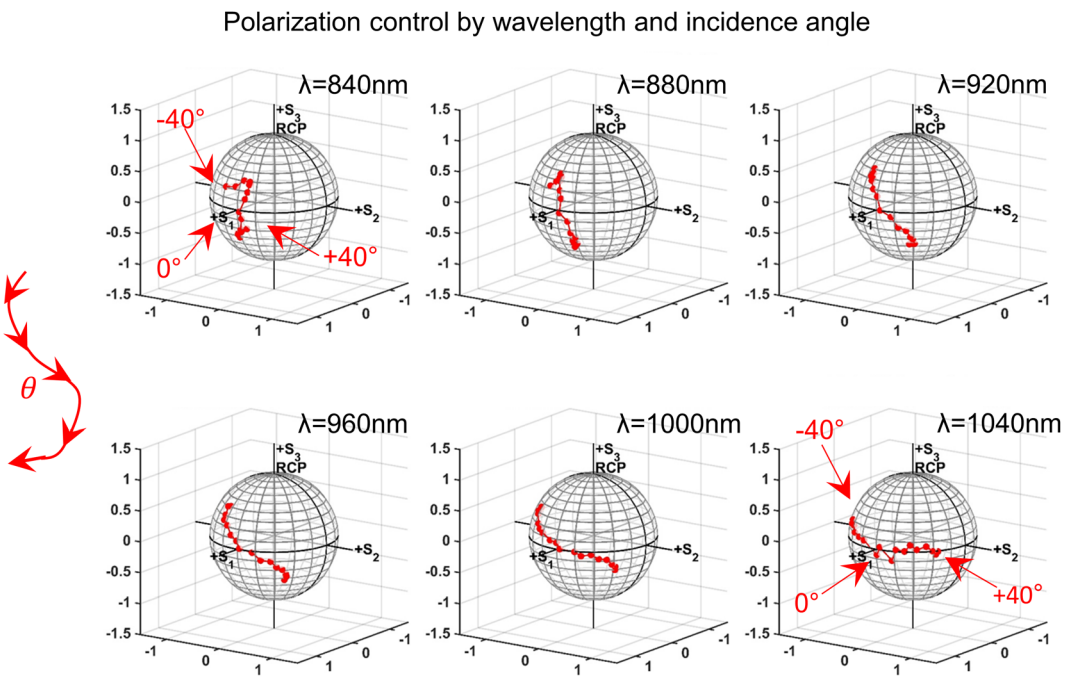

Fig. 6 Evolution of the output polarization vector on the Poincaré sphere, tuned with the incidence angles from −40° to +40°, at different excitation wavelengths; the excitation light is always p-polarized.

enhancement of S_3, which reaches values of ±0.5. The polarization state "walks" along the meridian $S_2 \sim 0$, meaning that it is a right or left elliptical polarization, with respect to the predominant horizontal long axis. The CD_{ext} resonance is broad, but as the wavelength is further increased, the ellipse long axis is tilted towards diagonals, and the circular polarization degree decreases as S_2 increases. Finally, at 1040 nm, the state stays almost linearly polarized, while its polarization can be gradually changed, following a route along the equator.

We next visualize the coupling mechanism from the near-field to the far-field, at 1000 nm. We excite the unit cell with p-polarization, LCP or RCP from the top; the incidence plane is given by the z-direction and a vector perpendicular to the asymmetry, $\vec{s}$. Fig. S1† shows that the increase of the incidence angle to $|\theta| = 30°$ leads to larger absorption in the plasmonic shell; however, the "total" absorption is largely similar at opposite incidence angles. Extrinsic CD is what is further reflected in the output polarization state because of different interactions between LCP and RCP. In Fig. S2†, we investigated the direction and polarization behaviour of the electric field vector; the white dashed line denotes the substrate surface. As expected, linear polarization at 0° keeps oscillating in line in both transmitted and reflected fields. Increasing the absolute incidence angle to 30° leads to larger coupling with the metasurface, indicated by the strongly enhanced electric field vector above the substrate, with complex near-field behaviour around the asymmetric plasmonic shell. With the switching between +30° and −30°, the transmitted field changes both the handedness and diagonal ellipse tilt. This agrees with the experiment where both S_2 and S_3 flip signs in a broad range around the resonance. Finally, extrinsic chirality affects the transmitted intensity and polarization, and we can visualize the coupling with RCP and LCP polarizations, observed in the first CD_{ext} experiment. At $\theta = -30°$, LCP light is strongly absorbed (also seen in Fig. 3b), while RCP is transmitted better. Indeed, below the metasurface, the intensity for RCP excitation is higher than that for LCP, which also agrees with the positive value of S_3 observed in the experiment. This feature is then inverted for $\theta = +30°$. Moreover, apart from coupling with circular polarizations at oblique incidence, we believe that the symmetry of our system could be broken even under normal incidence, with asymmetric helical beams carrying orbital angular momentum.[62] Therefore, we envision that such simple asymmetric metasurface geometries have potential in the hot topic of helical dichroism.[63]

3 Conclusion

We have reported on extrinsic chirality and widely tuneable Stokes parameters in simple, low-cost metasurfaces made of asymmetric gold semishells. Starting from measurements of circular dichroism at extinction, we gained insight into the coupling of the metasurface with LCP and RCP; we investigated how the incidence angle and wavelength affect the metamaterial CD resonances in the near-infrared range. We then showed the consequences of the asymmetry on the transmitted field polarization control. We excited the sample with linear polarization and mapped the Stokes parameters over wide ranges of wavelength and incidence angles. The S_3 parameter is strongly related to the observed extinction CD, and different paths on the Poincaré sphere can evolve with hyperspectral tuning of the incidence angle. The simulated electromagnetic coupling agrees well with the experiments, and the geometry can be further used for the coupling of emitters.

We previously proposed NSL-based geometries for the manipulation of polarization of the emitted field; as seen in ref. 50, we simulated the far-field distribution and polarization for a set of electric dipoles coupled with asymmetric metasurfaces. We observed high polarization degree in the emission, which followed the oblique emission governed by extrinsic chirality. We believe that the present work gives the first experimental proof that the state of output polarizations can be easily manipulated in our low-cost samples and that the coupling mechanisms follow the resonant extrinsic chiral behaviour of such simple geometries. The coupling of a plasmonic layer with molecules emitting in the near-infrared range could be done by doping the substrate below the metasurface, or by burying the metasurface into a dielectric layer doped with emitters. Moreover, given the good numerical model, NSL parameters can now be optimized to give higher CD and lead to circular polarizations of higher purity. Finally, we believe that the simple metasurface arrangement based on a thin asymmetric plasmonic semishell can lead to scalable plasmonic–photonic components for chiro-optical manipulation in the near- and far-fields.

Conflicts of interest

There are no conflicts to declare.

Acknowledgements

A. B. acknowledges LASAFEM Sapienza Università di Roma Infrastructure Project No. MA31715C8215A268 and Sapienza Large Research Project 2022 No. RG1221816B6FA2E9, PRIN 2022 PNRR Project INSPIRE n. P2022LETN5 founded by European Union - Next Generation EU. E. P. acknowledges the RTDa–PON "ricerca e innovazione" 2014–2020 for financial and mobility support. T.C. acknowledges the financial support of the Department of Physics and Astronomy through the project "PLANQ" PRD-BIRD-2022-Cesca.

References

1 F. A. A. Nugroho, D. Albinsson, T. J. Antosiewicz and C. Langhammer, *ACS Nano*, 2020, **14**, 2345–2353.
2 Y. Wang, C. Zhao, J. Wang, X. Luo, L. Xie, S. Zhan, J. Kim, X. Wang, X. Liu and Y. Ying, *Sci. Adv.*, 2021, **7**, eabe4553.

3 S. A. Khan, N. Z. Khan, Y. Xie, M. T. Abbas, M. Rauf, I. Mehmood, M. Runowski, S. Agathopoulos and J. Zhu, *Adv. Opt. Mater.*, 2022, **10**, 2200500.
4 S. I. Bozhevolnyi and N. A. Mortensen, *Nanophotonics*, 2017, **6**(5), 1185–1188.
5 J. Zhang, M. ElKabbash, R. Wei, S. C. Singh, B. Lam and C. Guo, *Light: Sci. Appl.*, 2019, **8**, 53.
6 A. J. Traverso, J. Huang, T. Peyronel, G. Yang, T. G. Tiecke and M. H. Mikkelsen, *Optica*, 2021, **8**(2), 202–207.
7 G. Li, X. Du, L. Xiong and X. Yang, *Adv. Opt. Mater.*, 2023, **11**, 2301205.
8 J. Bai, C. Wang, X. Chen, A. Basiri, C. Wang and Yu Yao, *Photonics Res.*, 2019, **7**, 1051–1060.
9 E. Petronijevic, A. Belardini, G. Leahu, R. Li Voti and C. Sibilia, *Opt. Mater. Express*, 2022, **12**(7), 2426–2937.
10 H. S. Khaliq, A. Nauman, J.-W. Lee and H.-R. Kim, *Adv. Opt. Mater.*, 2023, **11**, 2300644.
11 Y. Zhao, A. N. Askarpour, L. Sun, J. Shi, X. Li and A. Alù, *Nat. Commun.*, 2017, **8**, 14180.
12 J. García-Guirado, M. Svedendahl, J. Puigdollers and R. Quidant, *Nano Lett.*, 2018, **18**(10), 6279–6285.
13 Y. Y. Lee, R. M. Kim, S. W. Im, M. Balamurugan and K. T. Nam, *Nanoscale*, 2020, **12**, 58–66.
14 Y. Liu, Z. Wu, P. S. Kollipara, R. Montellano, K. Sharma and Y. Zheng, *ACS Nano*, 2021, **15**(4), 6448–6456.
15 M. Cen, J. Wang, J. Liu, H. He, K. Li, W. Cai, T. Cao and Y. J. Liu, *Adv. Mater.*, 2022, **34**, 2203956.
16 W. Cao, X. Yang and J. Gao, *Sci. Rep.*, 2017, **7**, 8841.
17 A. Pors, M. G. Nielsen and S. I. Bozhevolnyi, *Optica*, 2015, **2**(8), 716–723.
18 Y. Yang, H. Kim, T. Badloe and J. Rho, *Nanophotonics*, 2022, **11**(17), 4123–4133.
19 C. Chen, S. Gao, W. Song, H. Li, S.-N. Zhu and T. Li, *Nano Lett.*, 2021, **21**, 1815–1821.
20 Y. Chen, X. Yang and J. Gao, *Light: Sci. Appl.*, 2018, **7**, 84.
21 H.-T. Lin, Y.-Y. Hsu, P.-J. Cheng, W.-T. Wang, S.-W. Chang and M.-H. Shih, *Nanoscale Adv.*, 2022, **4**, 2428–2434.
22 L. Li, J. Wang, L. Kang, W. Liu, L. Yu, B. Zheng, M. L. Brongersma, D. H. Werner, S. Lan, Y. Shi, Y. Xu and X. Wang, *ACS Nano*, 2020, **14**, 16634–16642.
23 Y. Liang, H. Lin, K. Koshelev, F. Zhang, Y. Yang, J. Wu, Y. Kivshar and B. Jia, *Nano Lett.*, 2021, **21**(2), 1090–1095.
24 V. K. Valev, J. J. Baumberg, B. De Clercq, N. Braz, X. Zheng, E. J. Osley, S. Vandendriessche, M. Hojeij, C. Blejean, J. Mertens, C. G. Biris, V. Volskiy, M. Ameloot, Y. Ekinci, G. A. E. Vandenbosch, P. A. Warburton, V. V. Moshchalkov, N. C. Panoiu and T. Verbiest, *Adv. Mater.*, 2014, **26**, 4074–4081.
25 J. T. Collins, D. C. Hooper, A. G. Mark, C. Kuppe and V. K. Valev, *ACS Nano*, 2018, **12**(6), 5445–5451.
26 Y. Kan, S. K. H. Andersen, F. Ding, S. Kumar, C. Zhao and S. I. Bozhevolnyi, *Adv. Mater.*, 2020, **32**, 1907832.
27 D. Schanne, S. Suffit, P. Filloux, E. Lhuillier and A. Degiron, *Phys. Rev. Appl.*, 2020, **14**, 064077.
28 Y. Sang and M. Liu, *Chem. Sci.*, 2022, **13**, 633.
29 P. Kumar, T. Vo, M. Cha, A. Visheratina, J. Kim, W. Xu, J. Schwartz, A. Simon, D. Katz, V. P. Nicu, E. Marino, W. J. Choi, M. Veksler, S. Chen, C. Murray, R. Hovden, S. Glotzer and N. A. Kotov, *Nature*, 2023, **615**, 418–424.
30 R. Ogier, Y. Fang, M. Svedendahl, P. Johansson and M. Käll, *ACS Photonics*, 2014, **1**(10), 1074–1081.
31 E. S. A. Goerlitzer, R. Mohammadi, S. Nechayev, K. Volk, M. Rey, P. Banzer, M. Karg and N. Vogel, *Adv. Mater.*, 2020, **32**, 2001330.
32 X. Zhao, J. Wen, L. Li, Y. Wang, D. Wang, L. Chen, Y. Zhang and Y. Du, *J. Appl. Phys.*, 2019, **126**, 141101.
33 Y. Wang, M. Zhang, Y. Lai and L. Chi, *Nano Today*, 2018, **22**, 36–61.
34 A. K. Singh, K. K. Mandal, Y. Gupta, V. S. Abhay Anand, L. Eswaramoorthy, B. Kumar, A. Kala, S. Dixit, V. G. Achanta and A. Kumar, *Phys. Rev. Appl.*, 2023, **19**, 044012.
35 A. Nemiroski, M. Gonidec, J. M. Fox, P. Jean-Remy, E. Turnage and G. M. Whitesides, *ACS Nano*, 2014, **8**(11), 11061–11070.
36 Y. Guan, Z. Wang, B. Ai, C. Chen, W. Zhang, Y. Wang and G. Zhang, *ACS Appl. Mater. Interfaces*, 2020, **12**(44), 50192–50202.
37 X. Yang, Y. Liu, F. Chen, Q. Lin, R. Chikkaraddy, S. Huang, S. Xian, Y. Hou, J. Du, L. Xia and C. Du, *Rare Met.*, 2024, **43**(2), 723–735.
38 Y. He, K. Lawrence, W. Ingram and Y. Zhao, *Chem. Commun.*, 2016, **52**, 2047.
39 Y. Hou, H. M. Leung, C. T. Chan, J. Du, H. L. Chan and D. Y. Lei, *Adv. Funct. Mater.*, 2016, **26**, 7807–7816.
40 B. Ai, H. M. Luong and Y. Zhao, *Nanoscale*, 2020, **12**, 2479–2491.
41 J. Qin, L. Deng, T. Kang, L. Nie, H. Feng, H. Wang, R. Yang, X. Liang, T. Tang, J. Shen, C. Li, H. Wang, Y. Luo, G. Armelles and L. Bi, *ACS Nano*, 2020, **14**(3), 2808–2816.
42 A. Belardini, M. Centini, G. Leahu, D. C. Hooper, R. Li Voti, E. Fazio, J. W. Haus, A. Sarangan, V. K. Valev and C. Sibilia, *Sci. Rep.*, 2016, **6**, 31796.
43 G. Leahu, E. Petronijevic, A. Belardini, M. Centini, C. Sibilia, T. Hakkarainen, E. Koivusalo, M. Rizzo Piton, S. Suomalainen and M. Guina, *Adv. Opt. Mater.*, 2017, **5**(16), 1601063.
44 T. Hakkarainen, E. Petronijevic, M. Rizzo Piton and C. Sibilia, *Sci. Rep.*, 2019, **9**, 5040.
45 E. Petronijevic, M. Centini, A. Belardini, G. Leahu, T. Hakkarainen and C. Sibilia, *Opt. Express*, 2017, **25**(13), 14148.
46 E. Petronijevic, A. Belardini, G. Leahu, T. Hakkarainen, M. Rizzo Piton, E. Koivusalo and C. Sibilia, *Sci. Rep.*, 2021, **11**, 4316.
47 E. Petronijevic, S. A. Dereshgi, M. C. Larciprete, M. Centini, C. Sibilia and K. Aydin, *ACS Appl. Nano Mater.*, 2022, **5**(4), 5609–5616.
48 E. Petronijevic, G. Leahu, R. Li Voti, A. Belardini, C. Scian, N. Michieli, T. Cesca, G. Mattei and C. Sibilia, *Appl. Phys. Lett.*, 2019, **114**, 053101.

49 G. Leahu, E. Petronijevic, R. Li Voti, A. Belardini, T. Cesca, G. Mattei and C. Sibilia, *Adv. Opt. Mater.*, 2021, **9**, 2100670.
50 E. Petronijevic, A. Belardini, T. Cesca, C. Scian, G. Mattei and C. Sibilia, *Phys. Rev. Appl.*, 2021, **16**(1), 014003.
51 M. C. Giordano, A. Foti, E. Messina, P. G. Gucciardi, D. Comoretto and F. Buatier de Mongeot, *ACS Appl. Mater. Interfaces*, 2016, **8**, 6629–6638.
52 A. Belardini, A. Benedetti, M. Centini, G. Leahu, F. Mura, S. Sennato, C. Sibilia, V. Robbiano, M. C. Giordano, C. Martella, D. Comoretto and F. Buatier de Mongeot, *Adv. Opt. Mater.*, 2014, **2**, 208–213.
53 L. Zagaglia, S. Zanotti, M. Minkov, M. Liscidini, D. Gerace and L. C. Andreani, *Opt. Lett.*, 2023, **48**(19), 5017–5020.
54 Z. El-Ansary, H. P. Ram Kumar, B. Brioual, E. Petronijevic, T. Cesca, C. Scian, G. Mattei, M. El Hasnaoui, C. Sibilia and A. Belardini, *Opt. Quantum Electron.*, 2023, **55**, 627.
55 E. Plum, X.-X. Liu, V. A. Fedotov, Y. Chen, D. P. Tsai and N. I. Zheludev, *Phys. Rev. Lett.*, 2009, **102**, 113902.
56 L. Mao, K. Liu, S. Zhang and T. Cao, *ACS Photonics*, 2020, **7**(2), 375–383.
57 T. Cao, L. Mao, H. Fan, M. Lian, J. Jia, Y. Su and H. Ren, *Adv. Opt. Mater.*, 2023, **11**, 2202239.
58 H. Ali, E. Petronijevic, G. Pellegrini, C. Sibilia and L. C. Andreani, *Opt. Express*, 2023, **31**(9), 14196–14211.
59 L. Cerdán, L. Zundel and A. Manjavacas, *ACS Photonics*, 2023, **10**(6), 1925–1935.
60 B. Lyu, Y. Li, Q. Jia, H. Li, G. Yang, F. Cao, S. Kou, D. Liu, T. Cao, G. Li and J. Shi, *Laser Photonics Rev.*, 2023, **17**, 2201004.
61 Lumerical Solutions, Inc. **https://www.lumerical.com/tcad-products/fdtd/**.
62 J. Bégin, A. Jain, A. Parks, F. Hufnagel, P. Corkum, E. Karimi, T. Brabec and R. Bhardwaj, *Nat. Photonics*, 2023, **17**, 82–88.
63 J. Ni, S. Liu, G. Hu, Y. Hu, Z. Lao, J. Li, Q. Zhang, D. Wu, S. Dong, J. Chu and C. Qiu, *ACS Nano*, 2021, **15**(2), 2893–2900.